

Modulating Charge Separation with Hexagonal Boron Nitride Mediation in Vertical Van der Waals Heterostructures

Christy Roshini Paul Inbaraj, Roshan Jesus Mathew, Rajesh Kumar Ulaganathan, Raman Sankar, Monika Kataria, Hsia Yu Lin, Hao-Yu Cheng, Kung-Hsuan Lin, Hung-I Lin, Yu-Ming Liao, Fang Cheng Chou, Yit-Tsong Chen, Chih-Hao Lee, and Yang-Fang Chen*



Cite This: *ACS Appl. Mater. Interfaces* 2020, 12, 26213–26221



Read Online

ACCESS |



Metrics & More



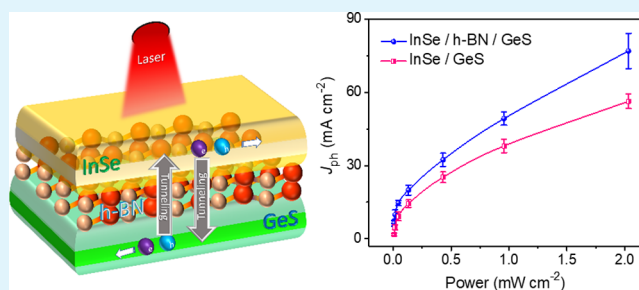
Article Recommendations



Supporting Information

ABSTRACT: Tuning the optical and electrical properties by stacking different layers of two-dimensional (2D) materials enables us to create unusual physical phenomena. Here, we demonstrate an alternative approach to enhance charge separation and alter physical properties in van der Waals heterojunctions with type-II band alignment by using thin dielectric spacers. To illustrate our working principle, we implement a hexagonal boron nitride (h-BN) sieve layer in between an InSe/GeS heterojunction. The optical transitions at the junctions studied by photoluminescence and the ultrafast pump–probe technique show quenching of emission without h-BN layers exhibiting an indirect recombination process. This quenching effect due to strong interlayer coupling was confirmed with Raman spectroscopic studies. In contrast, h-BN layers in between InSe and GeS show strong enhancement in emission, giving another degree of freedom to tune the heterojunction property. The two-terminal photoresponse study supports the argument by showing a large photocurrent density for an InSe/h-BN/GeS device by avoiding interlayer charge recombination. The enhanced charge separation with h-BN mediation manifests a photoresponsivity and detectivity of $9 \times 10^2 \text{ A W}^{-1}$ and 3.4×10^{14} Jones, respectively. Moreover, a photogain of 1.7×10^3 shows a high detection of electrons for the incident photons. Interestingly, the photovoltaic short-circuit current is switched from positive to negative, whereas the open-circuit voltage changes from negative to positive. Our proposed enhancement of charge separation with 2D-insulator mediation, therefore, provides a useful route to manipulate the physical properties of heterostructures and for the future development of high-performance optoelectronic devices.

KEYWORDS: *van der Waals heterostructure, monochalcogenide, carrier separation, insulator mediation, photodetector*



INTRODUCTION

The never-ending thirst for better performing electronic devices always keeps the researchers engrossed in tuning the properties of recently revolutionizing two-dimensional (2D) materials. Numerous ways are available to engineer the property of 2D materials such as applying strain,¹ contact electrode engineering,² surface functionalization,³ doping a ternary element,^{4,5} and interfacing different materials.⁶ Although many methods have been studied deeply, interfacing or coupling different 2D materials to form heterostructures have been appealing due to their increasing demand in optoelectronic devices.^{7,8} Unlike three-dimensional bulk heterostructures, the attractive features of 2D materials to thin down to an atomic layer, strong light–matter interaction, and their high flexibility intrigue the work on 2D heterostructures.^{9,10} Starting from graphene till chalcogenides, there have been many reports on both the lateral (materials interface along one-dimension) and vertical (materials overlap one above the other interfacing along two-dimensions) heterostructures.⁹ Among them, the most well-studied combinations include MoS₂/WS₂, MoS₂/WSe₂,

MoTe₂/MoS₂, and other transition-metal dichalcogenides for their applications in transistors, photodetectors, rectifiers, light-emitting diodes, lasers, and so forth.^{9,11–14} However, very few studies have been carried out on the class of monochalcogenide-based heterostructures.

To modulate the physical properties of van der Waals heterostructures, in this study, we propose a new approach to enhance charge carrier separation by inserting a thin insulating layer in between a 2D p–n junction with type-II band alignment. To illustrate our proposed working principle, for the present investigation, we have chosen the monochalcogenides, indium selenide (InSe) and germanium sulfide (GeS) for

Received: April 2, 2020

Accepted: May 13, 2020

Published: May 13, 2020



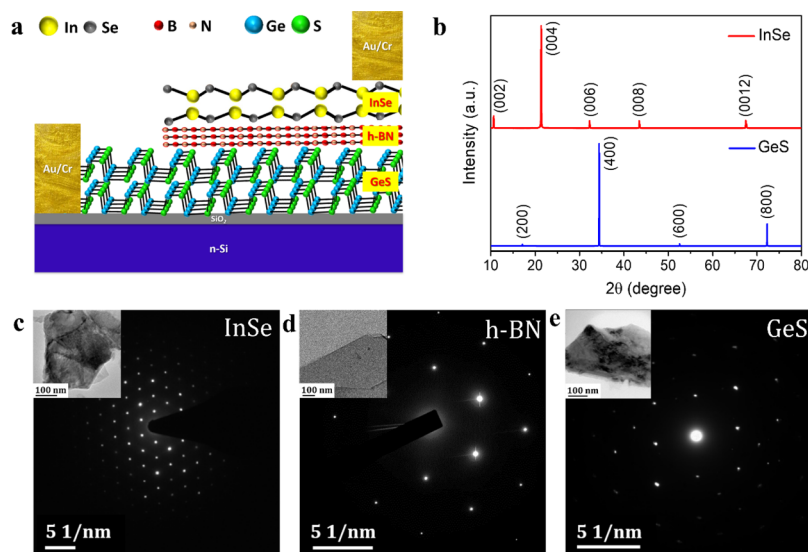


Figure 1. Material characterization of the crystals. (a) Schematic of the InSe/h-BN/GeS heterostructure device. (b) XRD pattern of the InSe and GeS crystals. (c–e) SAED pattern of the InSe, h-BN, and GeS single crystals with the inset showing their respective TEM images.

making vertical heterostructures. There have been recent reports on the n-type semiconductor, InSe, as it exhibits high electron mobility in the order of $10^3 \text{ cm}^2/\text{V s}$ due to their small electron effective mass which is approximately $0.131m_0$.^{5,15,16} InSe is a direct bandgap ($\sim 1.27 \text{ eV}$) semiconductor above 6 nm thickness and the bandgap remains the same, but below 6 nm, it changes to indirect due to quantum confinement effect.¹⁷ On the other hand, the bandgap of GeS varies in the range of $\sim 1.55\text{--}1.65 \text{ eV}$, and it is a p-type semiconductor.¹⁸ Although InSe and GeS are separately studied as photodetectors, there was no report so far of coupling the n-InSe and p-GeS forming a heterostructure. Based on the literature, fusing InSe and GeS will result in type-II band alignment due to their energy levels forming a p–n junction. The charge separation usually takes place in a type-II p–n junction, but the interlayer coupling can form tightly bound excitons and greatly reduce charge separation. To tune the physical property, here we introduce a dielectric spacer hexagonal boron nitride (h-BN) in between InSe and GeS. The crystal structure of h-BN is similar to graphene and can be exfoliated into thin layers.^{19,20} They have a wide bandgap of around 6 eV and are excellent dielectric materials,^{19,20} which have been widely used as substrates for fabricating high-performance devices, including as a dielectric for top-gated devices, as a tunneling barrier in graphene devices, and as a protecting layer for channel encapsulation.^{19,21,22}

In the present work, we focus on the structures by fabricating InSe/GeS and InSe/h-BN/GeS heterostructures on the SiO_2/Si substrate. The optical properties at these junctions have been studied using photoluminescence (PL) and ultrafast pump–probe measurements, which reveal an important fact that the strong interlayer coupling between layers can be modulated by the introduction of the h-BN spacer. Besides, the quenching effect due to strong interlayer coupling was further confirmed by Raman spectroscopy. InSe/GeS and InSe/h-BN/GeS heterostructure devices have been studied for their performance as a photodetector. Although the reverse bias operation gives better photodetection due to the large depletion layer in the p–n junction, it possesses significant electronic noise due to avalanche effects. To reduce the electronic noise and enhance the charge separation in the forward bias condition, we use h-

BN spacers in the device to avoid interlayer charge recombination. The carrier transport mechanism has been studied in detail in both the heterostructures. It was found that the photogain of the InSe/h-BN/GeS device can be enhanced by 1 order of magnitude compared to the InSe/GeS device in addition to the enhancement in photoresponsivity and detectivity. Our approach is therefore very useful for the manipulation of physical properties and the generation of high-performance optoelectronic devices based on vertically stacked 2D heterojunctions.

RESULTS AND DISCUSSION

Figure 1a represents the schematic of the InSe/h-BN/GeS heterostructure device. The InSe and GeS single crystals were grown by the Bridgman technique and chemical vapor transport (CVT) method, respectively, as elaborated in the [Experimental Section](#). The layered crystal structures of InSe and GeS are shown in [Figures S1 and S2](#), respectively. The prominent diffraction peaks in the X-ray diffraction (XRD) pattern of the InSe and GeS crystals as shown in [Figure 1b](#) confirm their hexagonal (β phase) and orthorhombic crystal structure, respectively. The XRD peaks of InSe were indexed following the standard database (JCPDS PDF 34-1431) and the lattice constants were found to be $a = b = 0.4 \text{ nm}$ and $c = 1.69 \text{ nm}$. The lattice constants of GeS were determined as $a = 0.43 \text{ nm}$, $b = 1.04 \text{ nm}$, and $c = 0.36 \text{ nm}$ by indexing the XRD peaks according to the standard JCPDS PDF 00-051-1168. The crystalline structure of InSe, h-BN, and GeS was further confirmed with transmission electron microscopy (TEM) and selected area diffraction (SAED) pattern as presented in [Figure 1c–e](#) (inset represents the TEM images). The SAED pattern reveals the high crystallinity and the crystal structures of InSe and GeS as hexagonal and orthorhombic, respectively. [Figure 1d](#) depicts the hexagonal geometry of h-BN. Few-layered GeS flakes were achieved by mechanical exfoliation and transferred to the SiO_2/Si substrate by a polydimethylsiloxane (PDMS) stamp. The exfoliated h-BN flakes were transferred to the GeS flake using a micromanipulator, and the same method was used to transfer InSe to the h-BN/GeS stack and GeS for the InSe/GeS structure. The schematic and detail of each step involved in the

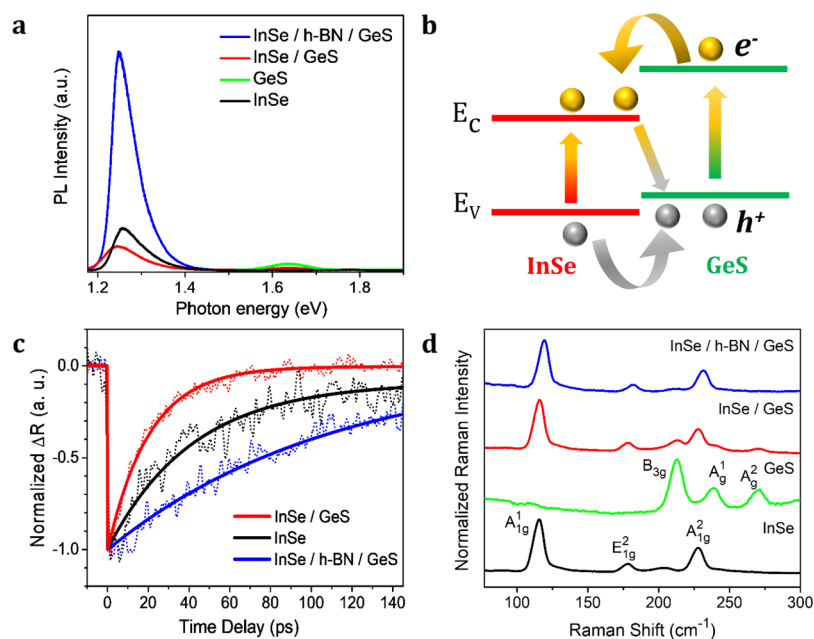


Figure 2. Optical studies of the heterostructures. (a) PL spectrum of the InSe/h-BN/GeS heterostructure. (b) Energy band diagram under photoexcitation. (c) Experimental data of the pump–probe measurements (in dotted lines) and the corresponding fitting curves (in solid lines). (d) Raman spectrum of the InSe/h-BN/GeS heterostructure.

dry transfer method are given in the [Supporting Information Note 2](#).

PL measurements were carried out to explore the optical properties of the InSe/GeS vertical heterostructure with and without h-BN as shown in [Figure 2a](#). The optical microscopy image and the atomic force microscopy (AFM) image along with the height profile of the samples used for the optical studies are as shown in [Figure S4](#). The zoomed-in portion of the PL spectrum and the peak fitting of the InSe peak are represented in [Figures S5 and S6](#), respectively. Few layered InSe shows a strong PL peak at 1.27 eV, whereas GeS at 1.62 eV ([Figure S5](#)), which is in accordance with the previous reports.^{17,18} The InSe/GeS heterostructure exhibits a strong interlayer coupling effect which is evident from the quenching of the PL peak and a negligible shift toward the lower energy at the junction. This significant PL quenching occurs due to the indirect recombination process at the interface.²³ [Figure 2b](#) depicts the band diagram at the InSe/GeS junction under photoexcitation. When the excitation laser is illuminated at the junction, both InSe and GeS layers absorb photons and generate excitons. The relaxation of these excitons at the interface undergoes an indirect non-radiative recombination process resulting in a quenched PL emission.²⁴ On the other hand, with h-BN as a spacer between InSe and GeS, the spatially indirect recombination at the interface is negligible and the strong interlayer coupling is suppressed by h-BN layers.²⁵ Because the number of h-BN layers is more than three, the direct exciton within the InSe layer remains intact, which is an indication of the lack of hole transfer and the PL intensity arising from the InSe layer in the InSe/h-BN/GeS structure is enhanced by 4–5 times when compared to the InSe layers alone ([Figure 2a](#)).

Ultrafast optical pump–probe measurements were conducted to study the dynamics of charge separation at the InSe/GeS interface with and without h-BN as the spacer. Because the photon energy of the pump was only higher than the bandgap of InSe, free carriers were only excited in the InSe

layer for all samples. By measuring the reflection changes of the probe pulses as a function of time delay, the carrier dynamics in InSe and interfacial charge transfer between InSe and GeS can be studied.^{26,27} [Figure 2c](#) reveals the transient reflection for the three samples and can be understood as follows. After the pump pulses excited carriers in InSe, the carrier density could decrease via carrier recombination through Auger recombination, surface recombination, and radiative recombination. Under the same experimental conditions, these intrinsic dynamics of carriers in InSe for the three samples are supposed to be the same. However, defect trappings and charge transfer could also decrease the carrier density in InSe and alter the transient reflectance. The resulting relaxation time, τ is the total effect of all relaxation processes through $\tau^{-1} = \sum \tau_i^{-1}$, where τ_i is the relaxation time for different channels.²⁸ That is, additional relaxation channels such as defect trappings or charge transfer, which are faster than the intrinsic relaxation, could shorten the relaxation time. In [Figure 2c](#), the summation of a single exponential decay function and a step function (in solid lines) was used to fit the experimental data (in dotted lines). The relaxation time constants of the exponential decay functions were 26 ± 6 , 44 ± 3 , and 180 ± 70 ps for InSe/GeS, InSe, and InSe/h-BN/GeS, respectively. Note that the errors of time constants do not result from the fitting ambiguity for a trace, but reflect the inhomogeneity for different measured spots. The shorter relaxation time in pure InSe (44 ps) compared with that of InSe/h-BN/GeS (180 ps) can be attributed to the better interface quality for InSe deposited on top of the h-BN layer, as reported in many previous studies.¹⁹ The relaxation time in InSe/GeS (26 ps) is the shortest, which supports the scenario that the hole-transfer process from InSe to GeS dramatically shortens the relaxation time. Assuming that the hole-transfer time, τ_{ht} dominantly shortens the relaxation time of InSe in InSe/h-BN/GeS ($\tau_{\text{InSe/h-BN}} = 180$ ps) to that of InSe in InSe/GeS ($\tau_{\text{InSe/GeS}} = 26$ ps). According to $\tau_{\text{InSe/GeS}}^{-1} = \tau_{\text{InSe/h-BN}}^{-1} + \tau_{ht}^{-1}$, the hole-transfer time, τ_{ht} from InSe to GeS can be estimated as 30 ps, which is on the same order of interfacial

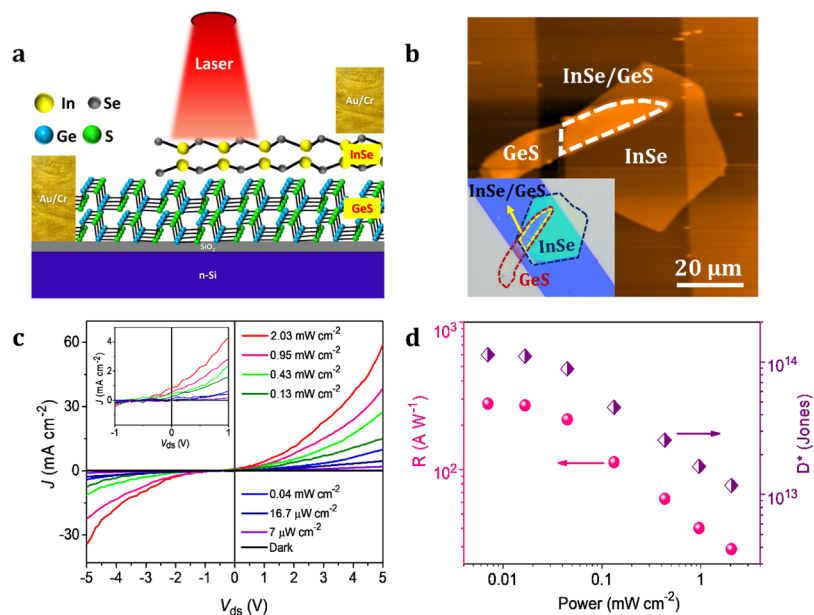


Figure 3. Electrical characteristics of the InSe/GeS device. (a) Schematic of the InSe/GeS heterostructure device. (b) AFM image of the InSe/GeS device and the inset represents the optical microscopy image with the junction region marked. (c) Current density as a function of applied voltage in the InSe/GeS device with the inset showing the region under zero bias. (d) Responsivity (R) and detectivity (D^*) of the device as a function of laser power ($V_{ds} = 5$ V).

charge-transfer times in semiconductors/ TiO_2 .^{28,29} Note that the transient reflection for InSe/GeS could not indicate the evolution of carrier density (or carrier lifetimes) in InSe or GeS. It is because the presence of transferred holes in GeS contributes positive signals to reflection, whereas the carriers in InSe contribute negative signals to reflection (see also Figure S7, Supporting Information Note 4). The lifetimes of carriers in individual layers are expected to be longer than the hole-transfer time but cannot be measured by our current experimental geometry.

Raman spectroscopic studies were employed to study the phonon vibrational modes at the junctions in the heterostructure as presented in Figure 2d. The isolated InSe flakes show prominent vibrations at 115 cm^{-1} (A_{1g}^1 , out-of-plane vibration), 178 cm^{-1} (E_{1g}^2 , in-plane vibration), and 228 cm^{-1} (A_{1g}^2 , out-of-plane vibration) in accordance with the previous reports.^{5,30} Isolated GeS flakes exhibit in-plane shear vibrational modes at 213 cm^{-1} (B_{3g}), 240 cm^{-1} (A_g^1), and 270 cm^{-1} (A_g^2) according to the previous reports.³¹ The significant quenching of Raman peaks belonging to GeS and the A_{1g}^2 mode of InSe (Figure S8) makes evident the strong interlayer coupling in the overlapping area.²⁴ A trivial shift in the InSe peaks and suppression of GeS peaks on inserting h-BN layers in between can be accounted to electron–phonon coupling or phonon–phonon coupling.^{32,33} Otherwise, the suppression of GeS peaks can be simply due to the reabsorption of the reflected beam by the top h-BN/InSe layer. Here, we point out that there do not exist any reports so far showing the variation of the Raman spectrum arising from 2D-semiconductor/h-BN/2D-semiconductor, which is an important and interesting topic awaiting more detailed study. The absence of any additional peaks at the heterostructure provides clear evidence that crystalline quality of the flakes was not degraded during the transfer process and no possible defects or contaminations were brought in all along with the dry transfer technique.³⁴

The p-type characteristics of GeS, where the majority carriers are holes and the n-type behavior of InSe, where electrons are

dominant are supported by the transfer curve measured for the GeS and InSe device separately in the field-effect transistor configuration as shown in Figure S9. The two-terminal device was fabricated with InSe/GeS hetero layers without h-BN forming a p–n junction diode. The schematic of the device structure with laser illumination is shown in Figure 3a. The AFM image of the InSe/GeS device with the junction region marked is represented in Figure 3b, and the inset shows the optical microscopy image. Figure S10 shows a typical height profile of the flakes; in this sample, the thickness of the InSe and GeS layers were determined to be ~ 30 and ~ 50 nm, respectively. The electrical characteristics of the InSe/GeS device were measured under laser ($\lambda = 633$ nm) illumination at different power intensities to study the photodetecting performance of the p–n diode formed. The drain–source current (I_{ds}) measured for the applied drain–source voltage (V_{ds}) in the forward bias condition was plotted as current density (J) by normalizing to the junction area as shown in Figure 3c. It is obvious from Figure 3c that the current density increases with the change in positive and negative bias under different laser power without saturation in the drain current. The rectification ratio ($I_{\text{forward}}/I_{\text{reverse}}$) calculated for the InSe/GeS device is ~ 11 with zero gate voltage, which is comparable to the previously reported 2D material-based vertical and lateral heterostructures.^{9,35–37} The enlarged view of the J – V_{ds} curve from -0.5 to $+0.5$ V is depicted in the inset of Figure 3c. It reveals a significant short-circuit current (I_{sc}) at zero bias with a small open-circuit voltage in the negative bias region, giving rise to a photovoltaic effect in the device similar to that in the AsP/InSe heterostructure reported earlier.³⁸ Unlike in the conventional photovoltaic device, the positive short-circuit current at high laser power (Figure S12a) can be attributed to the high resistance of InSe without any gate voltage. Consequently, large voltage drops at InSe and more photocurrent are generated from InSe when compared to the GeS channel, especially under 633 nm (~ 1.95 eV) laser illumination in a forward bias condition. To quantify the performance of the device as a

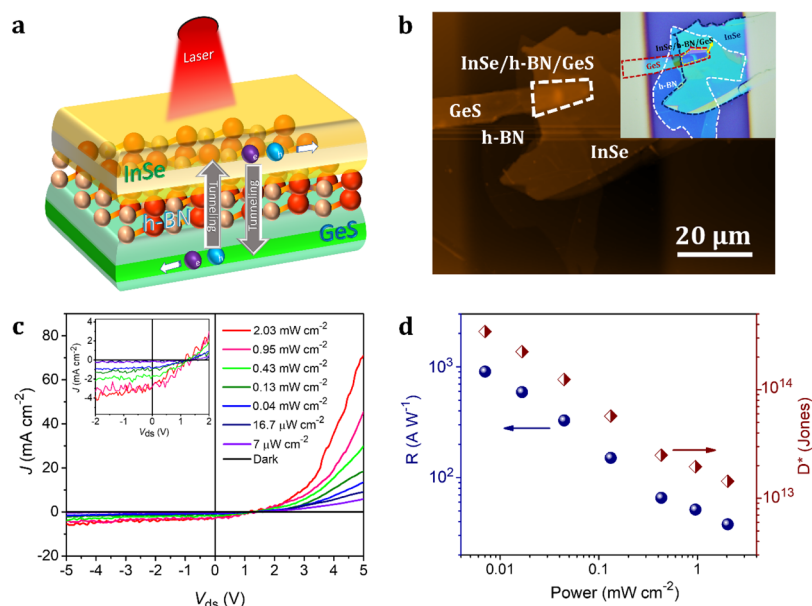


Figure 4. Electrical characteristics of the InSe/h-BN/GeS device. (a) Schematic of the charge separation and tunneling under laser illumination in the InSe/h-BN/GeS heterostructure device. (b) AFM image of the InSe/h-BN/GeS device and the inset represents the optical microscopy image with the junction region marked. (c) Current density as a function of applied voltage in the InSe/h-BN/GeS device with the inset showing the region under zero bias. (d) Responsivity (R) and detectivity (D^*) of the device at $V_{ds} = 5$ V.

photodetector, photoresponsivity (R) was estimated using the equation

$$R = \frac{I_{ph}}{P \times A} = \frac{I_{light} - I_{dark}}{P \times A} \quad (1)$$

where I_{ph} is the photocurrent generated as defined in the equation, P is the laser power density, and A is the active area of the device.^{5,39} Figure 3d shows the responsivity of the InSe/GeS device as a function of different laser power at $V_{ds} = 5$ V. Photoresponsivity enhances with a decrease in laser power and the responsivity in the InSe/GeS device reaches up to 2.7×10^2 $A W^{-1}$ ($V_{ds} = 5$ V, $P = 7 \mu W cm^{-2}$). Detectivity (D^*) is another parameter that implies the sensitivity of the device to detect weak signals. The value of detectivity was determined with the following equation⁵

$$D^* = \frac{(A\Delta f)^{1/2}}{NEP} \quad (2)$$

where A is the active device area, Δf is the measuring bandwidth which is inversely proportional to the response time of the device, and NEP is the noise equivalent power which signifies the feeble optical power that can be distinguished from noise. It is related to the root mean square noise current as $NEP = I_N/R$, where I_N is the noise current and proportional to the dark current (I_{dark}) according to the relation, $I_N^2 = 2eI_{dark}\Delta f$ (e is the electronic charge).⁵ Figure 3d represents the calculated D^* value as a function of different laser power and the maximum detectivity obtained at $V_{ds} = 5$ V and $P = 7 \mu W cm^{-2}$ is 1.1×10^{14} Jones.

To probe the effect of h-BN layers in the InSe/GeS device, the vertical heterostructure device of InSe/h-BN/GeS has been fabricated as mentioned earlier (Figure 1a). Figure 4a illustrates the InSe/h-BN/GeS device emphasizing the charge separation and the tunneling of charges through the h-BN barriers. AFM image of the InSe/h-BN/GeS device is represented in Figure 4b, specifying the junction area clearly and the inset depicts the

optical microscopy image. The thickness of the InSe, h-BN, and GeS layers are ~ 30 , ~ 4 , and ~ 50 nm, respectively, as shown in the height profile (Figure S11). The scanning electron microscopy (SEM) image of the device along with the elemental mapping is represented in Figure S13. The electrical characteristics of the device with laser illumination are plotted as current density versus applied bias as shown in Figure 4c. Similar to the InSe/GeS device, a laser with a wavelength of 633 nm was employed and the drain–source current measured in the forward bias condition. The current density (J) increases with the change in positive bias without saturation, whereas in the negative bias region, very feeble change is observed and nearly saturates, as revealed by Figure 4c. The rectification ratio ($I_{forward}/I_{reverse}$) estimated for the device is ~ 7 without the application of any gate voltage. Although it is better than heterojunctions such as pentacene/MoS₂ (~ 5)⁴⁰ and Ge/MoS₂ (~ 2),⁴¹ it is less than the InSe/GeS device. It signifies that carriers in the InSe/GeS junction undergo interlayer recombination following either the Langevin or Shockley–Read–Hall mechanism.¹⁰ In p–n junctions made of thin-layered materials, the tunneling-mediated interlayer recombination governs the current under forward bias.^{9,10} Therefore, the higher rectification ratio in InSe/GeS can be ascribed to the interlayer recombination taking place at the InSe and GeS interface, whereas h-BN layers as a thin barrier layer in between InSe and GeS avoids the carrier recombination resulting in lesser rectification ratio. The inset of Figure 4c depicts the enlarged view of the J – V_{ds} curve from -2 to $+2$ V. It discloses the observed negative short-circuit current (I_{sc}) at zero bias (Figure S12b) and a small positive open-circuit voltage manifesting a photovoltaic effect. The observed photovoltaic characteristic is in contrast to the InSe/GeS device where the short-circuit current is positive and open-circuit voltage is negative. This can be ascribed to the h-BN mediation layer which acts as a tunneling barrier to the device, allowing carrier tunneling. Besides, it favors hole transport and limits electron transport through it because of the barrier height arising from the band

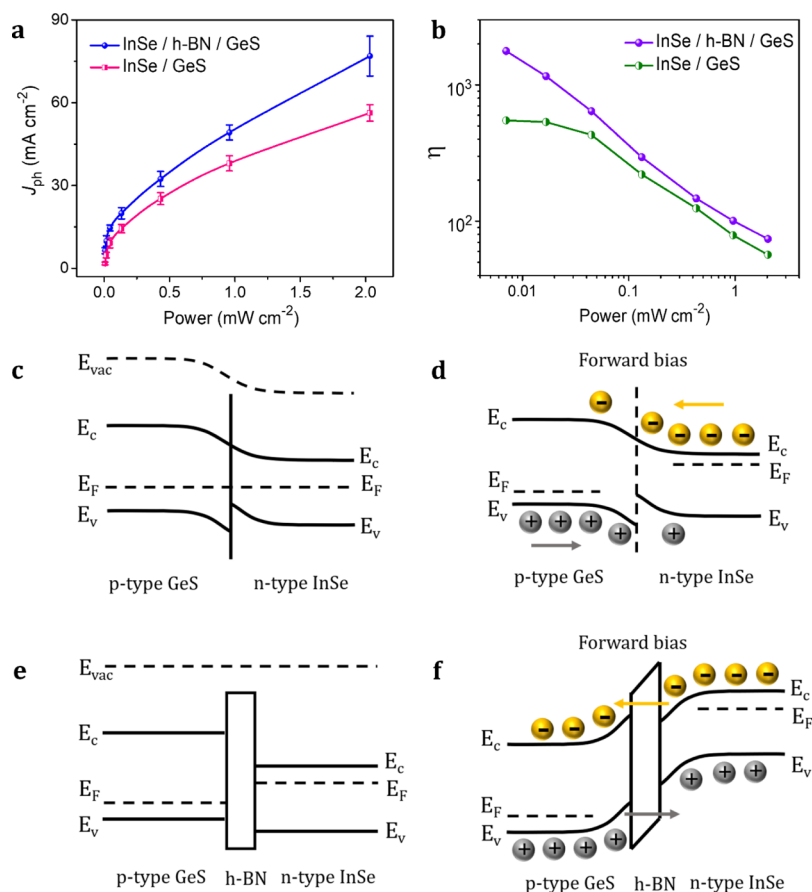


Figure 5. Carrier transport mechanism of the heterostructures. (a,b) Photocurrent density and photogain as a function of illuminated laser power at $V_{ds} = 5$ V in the InSe/GeS heterostructure device with and without h-BN mediation. (c,d) Energy band diagram of the p–n junction in the InSe/GeS device at zero bias and forward bias conditions, respectively. (e,f) Energy band diagram of the InSe/h-BN/GeS device at zero bias and forward bias conditions, respectively.

alignment between InSe and GeS at the interface.⁴² The photoresponsivity and detectivity of the device were calculated using eqs 1 and 2 and plotted as a function of illuminated laser power as shown in Figure 4d. The maximum responsivity and detectivity obtained at $V_{ds} = 5$ V, $P = 7 \mu\text{W cm}^{-2}$ is $9 \times 10^2 \text{ A W}^{-1}$ and 3.4×10^{14} Jones, respectively. These values are higher than those for the previously reported InSe heterostructure-based photodetectors.^{38,43} Thus, the results obtained from the optical and electrical study are consistent and the performance of the InSe/h-BN/GeS device is much higher than that of the InSe/GeS device. It can be credited to the h-BN layer as it acts as a sieve layer in between two semiconductors, efficiently limiting the electron passage and avoiding carrier recombination simultaneously.⁴² The photo-switching characteristics of both devices were presented in Figure S14.

To quantify the enhancement in photocurrent further, the photocurrent density (J_{ph}) at $V_{ds} = 5$ V was plotted as a function of illuminated laser power intensity (Figure 5a) for the InSe/GeS device with and without a h-BN mediation layer. The error limit for the variation in J_{ph} for a number of devices is included in Figure 5a. Another parameter, photogain (η) which quantifies the number of electrons detected for an incident photon was determined by the equation⁵

$$\eta = \frac{Rhc}{e\lambda} \quad (3)$$

(h —Planck's constant, c —the speed of light, and λ —wavelength of the light).⁵ The estimated photogain as a function of illuminated laser power at $V_{ds} = 5$ V is shown in Figure 5b. It reveals that the photogain is enhanced by one order in the presence of h-BN layers at the interface. It again affirms the increased charge separation and reduced recombination between the InSe and GeS layers due to h-BN mediation.⁴⁴ The mechanism of carrier transport for both InSe/GeS and InSe/h-BN/GeS devices is illustrated in Figure 5c–f. The energy levels of InSe, h-BN, and GeS and their band alignment are given in Figures S15 and S16, respectively. Initially, when the InSe/GeS (p–n) junction is formed, without any external bias a state of equilibrium is achieved due to the diffusion of holes to n-type InSe and electrons to p-type GeS at the junction (Figure 5c). This results in the formation of a depletion layer creating a built-in potential. In the forward bias condition, when an external bias is applied, above a certain threshold voltage the depletion layer becomes thin and carrier transport takes place at the junction. The electrons (majority carriers) flow from InSe to GeS and hole transfers from GeS to InSe leading to the significant current flow across the junction (Figure 5d). This transport mechanism matches well with the J – V_{ds} curve shown in Figure 3c. On the other hand, the InSe/h-BN/GeS heterostructure behaves like a semiconductor–insulator–semiconductor (SIS) diode. Figure 5e shows the band diagram under thermal equilibrium without external bias. When an external voltage is applied in the forward bias

condition, the carriers get accumulated at the interfaces (electrons at InSe/h-BN and holes at h-BN/GeS interface). When the applied bias is above the threshold voltage, a large number of accumulated charges tunnel across the h-BN layers leading to the significant current flow (Figure 5f). Therefore, with the applied forward bias, the h-BN layer behaves as a permanent tunneling barrier which avoids interlayer recombination and enables to enhance carrier separation leading to larger current flow in the InSe/h-BN/GeS heterostructure, which is consistent with the $J-V_{ds}$ curve shown in Figure 4c. Thus, the insertion of h-BN layers in between the InSe/GeS junction provides another degree of freedom to tune the physical properties of the heterostructure and paves way for the development of high-performance optoelectronic devices based on 2D materials.

CONCLUSIONS

We have provided an alternative approach to enhance charge carrier separation and modulate physical properties in vertically stacked van der Waals heterojunctions by a 2D insulating sieve layer. To demonstrate our proposed physical principle, we presented a meticulous study on the optical and electrical properties of the InSe/GeS p-n junction diode and the InSe/h-BN/GeS SIS diode. The PL and Raman spectroscopic studies reveal the strong interlayer coupling between the InSe and GeS heterostructure by quenching of PL and Raman peaks at the junction. The enhancement of PL with the insertion of h-BN layers gives clear evidence on the ability to tune the physical properties of InSe/GeS with h-BN as a spacer. The ultrafast pump-probe technique was employed to study the carrier dynamics of InSe at InSe/GeS and InSe/h-BN/GeS junctions, which is consistent with the observed changes in the PL. The electrical measurements of the InSe/GeS and InSe/h-BN/GeS device under laser illumination profess the higher photocurrent density observed in the InSe/h-BN/GeS device due to enhanced charge separation by the h-BN mediation. The maximum photoresponsivity, detectivity, and photogain of the InSe/h-BN/GeS device obtained are $9 \times 10^2 \text{ A W}^{-1}$, 3.4×10^{14} Jones, and 1.7×10^3 , respectively. Quite interestingly, the photovoltaic short-circuit current can be switched from positive to negative, whereas the open-circuit voltage changes from negative to positive. The energy band diagrams of both p-n junction (InSe/GeS) and SIS (InSe/h-BN/GeS) diodes were discussed in detail to understand the carrier tunneling mechanism through the h-BN layers. Thus, we have demonstrated a new degree of freedom to manipulate the physical properties of heterostructures, which is useful for the development of high-performance optoelectronic devices.

EXPERIMENTAL SECTION

Crystal Growth. *InSe.* InSe crystals were grown by the vertical Bridgman method. The molar mixture of 99.999% pure In and Se compounds (Sigma-Aldrich) was loaded in a conical quartz ampoule which was evacuated to 10^{-4} Pa. Batch homogenization followed by synthesis of single crystals was carried out in a horizontal furnace at 600 °C for 48 h. The heat-treatment was carried out for the melt in the ampoules at 850 °C for 24 h before pulling. The ampoule was lowered through a temperature gradient of 1 °C at a rate of 0.1 mm h^{-1} as the melt fills the ampoule tip. The as-grown InSe crystal with a dimension of 3 cm length and 1.2 cm diameter was obtained.

GeS. The CVT technique was used for GeS crystal growth. A three-zone furnace made of a quartz tube with each zone maintained at different temperatures (zone 1—600 °C, zone 2—577 °C, and zone 3—527 °C) was employed for growing crystals for a time period of 100

h. The dimensions of the furnace were 100 cm in length and the outer/inner diameter was 12/10 cm. Ge (99.999% pure) and S (99.999% pure) mixed in a stoichiometric 1:1 ratio were loaded in a quartz ampoule (length—32 cm; outer/inner diameter—2/1.8 cm) and sealed at a pressure of 10^{-4} Pa. The sealed ampoules were placed in the horizontal furnace and gradually heated to attain the specific temperature as mentioned earlier. The dimensions of the as-grown GeS crystal is $7.5 \times 6.5 \times 0.5 \text{ mm}^3$.

Device Fabrication. The InSe/h-BN/GeS and InSe/GeS heterostructures were prepared by the dry transfer technique. First, GeS flakes were mechanically exfoliated using Scotch tape and then transferred to SiO_2/Si substrate using a PDMS stamp. Then, thin flakes of h-BN (PolarTherm, Momentive) were exfoliated onto a PDMS film and placed exactly on the GeS flake using a custom made micromanipulator attached with the optical microscope. Similarly, InSe flakes were transferred onto h-BN/GeS stacks. The exfoliated flakes were scrutinized using optical microscopy (Olympus, BX 51M) equipped with Leica, DFC495 charge-coupled device. The thickness measurement for the flakes was carried out using AFM. To deposit electrodes, the TEM copper grid was employed as a shadow mask and located exactly on the heterostructure using the micromanipulator. The Cr/Au electrodes (7/70 nm) were deposited by the thermal evaporation technique.

Characterization Details. XRD of InSe and GeS was recorded using the X-ray diffractometer (X'Pert PRO-PANalytical) at room temperature with Cu $K\alpha$ radiation for the 2θ range from 10 to 80°. TEM was carried out with Philips Tecnai F30 field-emission gun transmission microscopy operating at 300 kV. The PL spectra were recorded by HORIBA Lab RAM HR spectrometer equipped with HORIBA Sincerity detector using excitation energy (E_{exc}) as 2.33 eV. Ultrafast optical pump-probe measurements were conducted by using a home-built setup. A detailed configuration can be found elsewhere.⁴⁵ The repetition rate of the pulses was 80 MHz. The photon energy of the pump and probe were centered at 1.57 and 1.60 eV, respectively. The powers of the pump and probe were 12 and 4 mW, respectively. The pump and probe beams were collinearly focused onto the sample with an objective lens with numerical aperture 0.95. The spot sizes were $\sim 700 \text{ nm}$. The Raman spectra of the heterostructure were measured using a Jodson micro-Raman spectrometer furnished with an optical microscope (Olympus CX41) and Jobin Won HORIBA S Drive-500 Sincerity detector. The excitation energy used was 2.33 eV and a grating of 1800 g mm^{-1} . In advance to the spectral acquisition, the spectrometer was calibrated to a Si peak (520 cm^{-1}). AFM imaging was carried out with Nanosurf Flex AFM, easyScan 2 V.3.1. A Keithley 2400 electrometer was employed to record the electrical characteristics of the device. He-Ne laser ($\lambda = 633 \text{ nm}$) was applied for measuring the photoresponse.

ASSOCIATED CONTENT

Supporting Information

The Supporting Information is available free of charge at <https://pubs.acs.org/doi/10.1021/acsami.0c06077>.

Crystal structure of InSe and GeS; vertical heterostructure fabrication; PL spectrum analysis; ultrafast pump-probe measurement; Raman spectrum analysis; transfer characteristics of the InSe and GeS device; AFM image of the device; analysis of the electrical measurement; SEM image of the device; photo-switching characteristics of the device; and energy levels of the crystals (PDF)

AUTHOR INFORMATION

Corresponding Author

Yang-Fang Chen — Department of Physics and Advanced Research Centre for Green Materials Science and Technology, National Taiwan University, Taipei 10617, Taiwan;

orcid.org/0000-0003-1203-5115; Email: yfchen@phys.ntu.edu.tw

Authors

Christy Roshini Paul Inbaraj – Department of Engineering and System Science, National Tsing Hua University, Hsinchu 30013, Taiwan; Nano-Science and Technology Program, Taiwan International Graduate Program, Academia Sinica, Taipei 11529, Taiwan; Department of Physics, National Taiwan University, Taipei 10617, Taiwan; orcid.org/0000-0002-8776-9917

Roshan Jesus Mathew – Department of Engineering and System Science, National Tsing Hua University, Hsinchu 30013, Taiwan; Nano-Science and Technology Program, Taiwan International Graduate Program and Institute of Atomic and Molecular Sciences, Academia Sinica, Taipei 11529, Taiwan; orcid.org/0000-0002-0913-6321

Rajesh Kumar Ulaganathan – Center for Condensed Matter Sciences, National Taiwan University, Taipei 10617, Taiwan; orcid.org/0000-0001-8886-6332

Raman Sankar – Center for Condensed Matter Sciences, National Taiwan University, Taipei 10617, Taiwan; Institute of Physics, Academia Sinica, Taipei 11529, Taiwan; orcid.org/0000-0003-4702-2517

Monika Kataria – Department of Physics and Advanced Research Centre for Green Materials Science and Technology, National Taiwan University, Taipei 10617, Taiwan; Institute of Atomic and Molecular Sciences and Molecular Science and Technology Program, Taiwan International Graduate Program, Academia Sinica, Taipei 10617, Taiwan; Department of Physics, National Central University, Chung-Li 320, Taiwan; orcid.org/0000-0003-4912-340X

Hsia Yu Lin – Department of Physics, National Taiwan University, Taipei 10617, Taiwan; orcid.org/0000-0002-0886-3367

Hao-Yu Cheng – Institute of Physics, Academia Sinica, Taipei 11529, Taiwan

Kung-Hsuan Lin – Institute of Physics, Academia Sinica, Taipei 11529, Taiwan

Hung-I Lin – Department of Physics, National Taiwan University, Taipei 10617, Taiwan; orcid.org/0000-0001-9849-3138

Yu-Ming Liao – Nano-Science and Technology Program, Taiwan International Graduate Program, Academia Sinica, Taipei 11529, Taiwan; Department of Physics, National Taiwan University, Taipei 10617, Taiwan; orcid.org/0000-0002-8696-7313

Fang Cheng Chou – Center for Condensed Matter Sciences, National Taiwan University, Taipei 10617, Taiwan

Yit-Tsong Chen – Institute of Atomic and Molecular Sciences, Academia Sinica, Taipei 10617, Taiwan; Department of Chemistry, National Taiwan University, Taipei 10617, Taiwan; orcid.org/0000-0002-6204-8320

Chih-Hao Lee – Department of Engineering and System Science, National Tsing Hua University, Hsinchu 30013, Taiwan; orcid.org/0000-0002-3898-6421

Complete contact information is available at:
<https://pubs.acs.org/10.1021/acsami.0c06077>

Author Contributions

The manuscript was written through the contributions of all authors. All authors have given approval to the final version of the manuscript.

Notes

The authors declare no competing financial interest.

ACKNOWLEDGMENTS

This work was funded by the “Advanced Research Center for Green Materials Science and Technology” from the Featured Area Research Center Program within the framework of the Higher Education Sprout Project by the Ministry of Education (109L9006) and the Ministry of Science and Technology in Taiwan (MOST 109-2634-F-002-042, MOST 108-2112-M-002-019). This project was partly funded by MOST (106-2119-M-002-035-MY3 and 108-2112-M-001-049-MY2). R.S and F.C.C both acknowledge Academia Sinica for the budget of AS-iMATE-109-13. C.R.P.I. would like to gratefully acknowledge the support of the Taiwan Internal Graduate Program (TIGP), Institute of Physics, Academia Sinica, Taipei, Taiwan, and National Tsing Hua University, Hsinchu, Taiwan.

REFERENCES

- (1) Dai, Z.; Liu, L.; Zhang, Z. Strain Engineering of 2D Materials: Issues and Opportunities at the Interface. *Adv. Mater.* **2019**, *31*, 1805417.
- (2) Schulman, D. S.; Arnold, A. J.; Das, S. Contact Engineering for 2D Materials and Devices. *Chem. Soc. Rev.* **2018**, *47*, 3037–3058.
- (3) Lei, S.; Wang, X.; Li, B.; Kang, J.; He, Y.; George, A.; Ge, L.; Gong, Y.; Dong, P.; Jin, Z.; Brunetto, G.; Chen, W.; Lin, Z.-T.; Baines, R.; Galvão, D. S.; Lou, J.; Barrera, E.; Banerjee, K.; Vajtai, R.; Ajayan, P. Surface Functionalization of Two-Dimensional Metal Chalcogenides by Lewis Acid-Base Chemistry. *Nat. Nanotechnol.* **2016**, *11*, 465–471.
- (4) Luo, P.; Zhuge, F.; Zhang, Q.; Chen, Y.; Lv, L.; Huang, Y.; Li, H.; Zhai, T. Doping Engineering and Functionalization of Two-Dimensional Metal Chalcogenides. *Nanoscale Horiz.* **2019**, *4*, 26–51.
- (5) Paul Inbaraj, C. R.; Gudelli, V. K.; Mathew, R. J.; Ulaganathan, R. K.; Sankar, R.; Lin, H. Y.; Lin, H.-I.; Liao, Y.-M.; Cheng, H.-Y.; Lin, K.-H.; Chou, F. C.; Chen, Y.-T.; Lee, C.-H.; Guo, G.-Y.; Chen, Y.-F. Sn-Doping Enhanced Ultrahigh Mobility In_{1-x}Sn_xSe Phototransistor. *ACS Appl. Mater. Interfaces* **2019**, *11*, 24269–24278.
- (6) Liu, X.; Hersam, M. C. Interface Characterization and Control of 2D Materials and Heterostructures. *Adv. Mater.* **2018**, *30*, 1801586.
- (7) Liu, Y.; Weiss, N. O.; Duan, X.; Cheng, H. C.; Huang, Y.; Duan, X. Van Der Waals Heterostructures and Devices. *Nat. Rev. Mater.* **2016**, *1*, 16042.
- (8) Duan, X.; Wang, C.; Pan, A.; Yu, R.; Duan, X. Two-Dimensional Transition Metal Dichalcogenides as Atomically Thin Semiconductors: Opportunities and Challenges. *Chem. Soc. Rev.* **2015**, *44*, 8859–8876.
- (9) Frisenda, R.; Molina-Mendoza, A. J.; Mueller, T.; Castellanos-Gomez, A.; Van Der Zant, H. S. J. Atomically Thin p-n Junctions Based on Two-Dimensional Materials. *Chem. Soc. Rev.* **2018**, *47*, 3339–3358.
- (10) Lee, C.-H.; Lee, G.-H.; Van Der Zande, A. M.; Chen, W.; Li, Y.; Han, M.; Cui, X.; Arefe, G.; Nuckolls, C.; Heinz, T. F.; Guo, J.; Hone, J.; Kim, P. Atomically Thin p-n Junctions with van Der Waals Heterointerfaces. *Nat. Nanotechnol.* **2014**, *9*, 676–681.
- (11) Furchi, M. M.; Pospischil, A.; Libisch, F.; Burgdörfer, J.; Mueller, T. Photovoltaic Effect in an Electrically Tunable Van der Waals Heterojunction. *Nano Lett.* **2014**, *14*, 4785–4791.
- (12) Cheng, R.; Li, D.; Zhou, H.; Wang, C.; Yin, A.; Jiang, S.; Liu, Y.; Chen, Y.; Huang, Y.; Duan, X. Electroluminescence and Photocurrent Generation from Atomically Sharp WSe₂/MoS₂ Heterojunction p-n Diodes. *Nano Lett.* **2014**, *14*, 5590–5597.
- (13) Gong, Y.; Lin, J.; Wang, X.; Shi, G.; Lei, S.; Lin, Z.; Zou, X.; Ye, G.; Vajtai, R.; Yakobson, B. I.; Terrones, H.; Terrones, M.; Tay, B. K.; Lou, J.; Pantelides, S. T.; Liu, Z.; Zhou, W.; Ajayan, P. M. Vertical and In-Plane Heterostructures from WS₂/MoS₂ Monolayers. *Nat. Mater.* **2014**, *13*, 1135–1142.
- (14) Ahn, J.; Jeon, P. J.; Raza, S. R. A.; Pezeshki, A.; Min, S. W.; Hwang, D. K.; Im, S. Transition Metal Dichalcogenide Heterojunction

PN Diode toward Ultimate Photovoltaic Benefits. *2D Mater.* **2016**, *3*, 045011.

(15) Sucharitakul, S.; Goble, N. J.; Kumar, U. R.; Sankar, R.; Bogorad, Z. A.; Chou, F.-C.; Chen, Y.-T.; Gao, X. P. A. Intrinsic Electron Mobility Exceeding $10^3 \text{ cm}^2/(\text{V s})$ in Multilayer InSe FETs. *Nano Lett.* **2015**, *15*, 3815–3819.

(16) Kress-Rogers, E.; Nicholas, R. J.; Portal, J. C.; Chevy, A. Cyclotron Resonance Studies on Bulk and Two-Dimensional Conduction Electrons in InSe. *Solid State Commun.* **1982**, *44*, 379–383.

(17) Mudd, G. W.; Svatek, S. A.; Ren, T.; Patanè, A.; Makarovskiy, O.; Eaves, L.; Beton, P. H.; Kovalyuk, Z. D.; Lashkarev, G. V.; Kudrynskiy, Z. R.; Dmitriev, A. I. Tuning the Bandgap of Exfoliated InSe Nanosheets by Quantum Confinement. *Adv. Mater.* **2013**, *25*, 5714–5718.

(18) Ramasamy, P.; Kwak, D.; Lim, D.-H.; Ra, H.-S.; Lee, J.-S. Solution Synthesis of GeS and GeSe Nanosheets for High-Sensitivity Photodetectors. *J. Mater. Chem. C* **2016**, *4*, 479–485.

(19) Dean, C. R.; Young, A. F.; Meric, I.; Lee, C.; Wang, L.; Sorgenfrei, S.; Watanabe, K.; Taniguchi, T.; Kim, P.; Shepard, K. L.; Hone, J. Boron Nitride Substrates for High-Quality Graphene Electronics. *Nat. Nanotechnol.* **2010**, *5*, 722–726.

(20) Gorbachev, R. V.; Riaz, I.; Nair, R. R.; Jalil, R.; Britnell, L.; Belle, B. D.; Hill, E. W.; Novoselov, K. S.; Watanabe, K.; Taniguchi, T.; Geim, A. K.; Blake, P. Hunting for Monolayer Boron Nitride: Optical and Raman Signatures. *Small* **2011**, *7*, 465–468.

(21) Mayorov, A. S.; Gorbachev, R. V.; Morozov, S. V.; Britnell, L.; Jalil, R.; Ponomarenko, L. A.; Blake, P.; Novoselov, K. S.; Watanabe, K.; Taniguchi, T.; Geim, A. K. Micrometer-Scale Ballistic Transport in Encapsulated Graphene at Room Temperature. *Nano Lett.* **2011**, *11*, 2396–2399.

(22) Britnell, L.; Gorbachev, R. V.; Jalil, R.; Belle, B. D.; Schedin, F.; Katsnelson, M. I.; Eaves, L.; Morozov, S. V.; Mayorov, A. S.; Peres, N. M. R.; Castro Neto, A. H.; Leist, J.; Geim, A. K.; Ponomarenko, L. A.; Novoselov, K. S. Electron Tunneling through Ultrathin Boron Nitride Crystalline Barriers. *Nano Lett.* **2012**, *12*, 1707–1710.

(23) Lee, I.; Rathi, S.; Lim, D.; Li, L.; Park, J.; Lee, Y.; Yi, K. S.; Dhakal, K. P.; Kim, J.; Lee, C.; Lee, G.-H.; Kim, Y. D.; Hone, J.; Yun, S. J.; Youn, D.-H.; Kim, G.-H. Gate-Tunable Hole and Electron Carrier Transport in Atomically Thin Dual-Channel $\text{WSe}_2/\text{MoS}_2$ Heterostructure for Ambipolar Field-Effect Transistors. *Adv. Mater.* **2016**, *28*, 9519–9525.

(24) Zhou, X.; Hu, X.; Zhou, S.; Song, H.; Zhang, Q.; Pi, L.; Li, L.; Li, H.; Lü, J.; Zhai, T. Tunneling Diode Based on $\text{WSe}_2/\text{SnS}_2$ Heterostructure Incorporating High Detectivity and Responsivity. *Adv. Mater.* **2018**, *30*, 1703286.

(25) Fang, H.; Battaglia, C.; Carraro, C.; Nemsak, S.; Ozdol, B.; Kang, J. S.; Bechtel, H. A.; Desai, S. B.; Kronast, F.; Unal, A. A.; Conti, G.; Conlon, C.; Palsson, G. K.; Martin, M. C.; Minor, A. M.; Fadley, C. S.; Yablonovitch, E.; Maboudian, R.; Javey, A. Strong Interlayer Coupling in van Der Waals Heterostructures Built from Single-Layer Chalcogenides. *Proc. Natl. Acad. Sci. U.S.A.* **2014**, *111*, 6198–6202.

(26) Yang, C.-Y.; Chia, C.-T.; Chen, H.-Y.; Gwo, S.; Lin, K.-H. Ultrafast Carrier Dynamics in GaN Nanorods. *Appl. Phys. Lett.* **2014**, *105*, 212105.

(27) Zhong, C.; Sangwan, V. K.; Kang, J.; Luxa, J.; Sofer, Z.; Hersam, M. C.; Weiss, E. A. Hot Carrier and Surface Recombination Dynamics in Layered InSe Crystals. *J. Phys. Chem. Lett.* **2019**, *10*, 493–499.

(28) Kuo, T.-R.; Liao, H.-J.; Chen, Y.-T.; Wei, C.-Y.; Chang, C.-C.; Chen, Y.-C.; Chang, Y.-H.; Lin, J.-C.; Lee, Y.-C.; Wen, C.-Y.; Li, S.-S.; Lin, K.-H.; Wang, D.-Y. Extended Visible to Near-Infrared Harvesting of Earth-Abundant $\text{FeS}_2\text{-TiO}_2$ Heterostructures for Highly Active Photocatalytic Hydrogen Evolution. *Green Chem.* **2018**, *20*, 1640–1647.

(29) Zhang, P.; Zhu, G.; Shi, Y.; Wang, Y.; Zhang, J.; Du, L.; Ding, D. Ultrafast Interfacial Charge Transfer of Cesium Lead Halide Perovskite Films CsPbX_3 ($X = \text{Cl, Br, I}$) with Different Halogen Mixing. *J. Phys. Chem. C* **2018**, *122*, 27148–27155.

(30) Carlone, C.; Jandl, S.; Shanks, H. R. Optical Phonons and Crystalline Symmetry of InSe. *Phys. Status Solidi A* **1981**, *103*, 123–130.

(31) Tan, D.; Lim, H. E.; Wang, F.; Mohamed, N. B.; Mouri, S.; Zhang, W.; Miyauchi, Y.; Ohfuchi, M.; Matsuda, K. Anisotropic Optical and Electronic Properties of Two-Dimensional Layered Germanium Sulfide. *Nano Res.* **2017**, *10*, 546–555.

(32) Jin, C.; Kim, J.; Suh, J.; Shi, Z.; Chen, B.; Fan, X.; Kam, M.; Watanabe, K.; Taniguchi, T.; Tongay, S.; Zettl, A.; Wu, J.; Wang, F. Interlayer Electron-Phonon Coupling in WSe_2/hBN Heterostructures. *Nat. Phys.* **2017**, *13*, 127–131.

(33) Du, L.; Zhao, Y.; Jia, Z.; Liao, M.; Wang, Q.; Guo, X.; Shi, Z.; Yang, R.; Watanabe, K.; Taniguchi, T.; Xiang, J.; Shi, D.; Dai, Q.; Sun, Z.; Zhang, G. Strong and Tunable Interlayer Coupling of Infrared-Active Phonons to Excitons in van der Waals Heterostructures. *Phys. Rev. B* **2019**, *99*, 205410.

(34) Tao, L.; Li, H.; Gao, Y.; Chen, Z.; Wang, L.; Deng, Y.; Zhang, J.; Xu, J.-B. Deterministic and Etching-Free Transfer of Large-Scale 2D Layered Materials for Constructing Interlayer Coupled van Der Waals Heterostructures. *Adv. Mater. Technol.* **2018**, *3*, 1700282.

(35) Zhang, K.; Zhang, T.; Cheng, G.; Li, T.; Wang, S.; Wei, W.; Zhou, X.; Yu, W.; Sun, Y.; Wang, P.; Zhang, D.; Zeng, C.; Wang, X.; Hu, W.; Fan, H. J.; Shen, G.; Chen, X.; Duan, X.; Chang, K.; Dai, N. Interlayer Transition and Infrared Photodetection in Atomically Thin Type-II $\text{MoTe}_2/\text{MoS}_2$ van Der Waals Heterostructures. *ACS Nano* **2016**, *10*, 3852–3858.

(36) Zheng, Z.; Yao, J.; Yang, G. Self-Assembly of the Lateral $\text{In}_2\text{Se}_3/\text{CuInSe}_2$ Heterojunction for Enhanced Photodetection. *ACS Appl. Mater. Interfaces* **2017**, *9*, 7288–7296.

(37) Li, M.-Y.; Shi, Y.; Cheng, C.-C.; Lu, L.-S.; Lin, Y.-C.; Tang, H.-L.; Tsai, M.-L.; Chu, C.-W.; Wei, K.-H.; He, J.-H. *Science* **2015**, *349*, 524–528.

(38) Wu, F.; Xia, H.; Sun, H.; Zhang, J.; Gong, F.; Wang, Z.; Chen, L.; Wang, P.; Long, M.; Wu, X.; Wang, J.; Ren, W.; Chen, X.; Lu, W.; Hu, W. AsP/InSe Van Der Waals Tunneling Heterojunctions with Ultrahigh Reverse Rectification Ratio and High Photosensitivity. *Adv. Funct. Mater.* **2019**, *29*, 1900314.

(39) Paul Inbaraj, C. R.; Mathew, R. J.; Haider, G.; Chen, T.-P.; Ulaganathan, R. K.; Sankar, R.; Bera, K. P.; Liao, Y.-M.; Kataria, M.; Lin, H.-I.; Chou, F. C.; Chen, Y.-T.; Lee, C.-H.; Chen, Y.-F. Ultra-High Performance Flexible Piezopotential Gated $\text{In}_{1-x}\text{Sn}_x\text{Se}$ Phototransistor. *Nanoscale* **2018**, *10*, 18642–18650.

(40) Jariwala, D.; Howell, S. L.; Chen, K.-S.; Kang, J.; Sangwan, V. K.; Filippone, S. A.; Turrissi, R.; Marks, T. J.; Lauhon, L. J.; Hersam, M. C. Hybrid, Gate-Tunable, van Der Waals p-n Heterojunctions from Pentacene and MoS_2 . *Nano Lett.* **2016**, *16*, 497–503.

(41) Sarkar, D.; Xie, X.; Liu, W.; Cao, W.; Kang, J.; Gong, Y.; Kraemer, S.; Ajayan, P. M.; Banerjee, K. A Subthermionic Tunnel Field-Effect Transistor with an Atomically Thin Channel. *Nature* **2015**, *526*, 91–95.

(42) Hattori, Y.; Taniguchi, T.; Watanabe, K.; Nagashio, K. Determination of Carrier Polarity in Fowler–Nordheim Tunneling. *ACS Appl. Mater. Interfaces* **2018**, *10*, 11732–11738.

(43) Chen, Z.; Zhang, Z.; Biscaras, J.; Shukla, A. A High Performance Self-Driven Photodetector Based on a Graphene/InSe/ MoS_2 Vertical Heterostructure. *J. Mater. Chem. C* **2018**, *6*, 12407–12412.

(44) Xie, C.; Mak, C.; Tao, X.; Yan, F. Photodetectors Based on Two-Dimensional Layered Materials Beyond Graphene. *Adv. Funct. Mater.* **2017**, *27*, 1603886.

(45) Lin, K.-H.; Cheng, H.-Y.; Yang, C.-Y.; Li, H.-W.; Chang, C.-W.; Chu, S.-W. Phonon Dynamics of Single Nanoparticles Studied Using Confocal Pump-Probe Backscattering. *Appl. Phys. Lett.* **2018**, *113*, 171906.